

# Digging Deep into the layers of CNNs: In Search of How CNNs Achieve View Invariance

Amr Bakry \*

amrbakry@cs.rutgers.edu

Mohamed Elhoseiny \*

m.elhoseiny@cs.rutgers.edu

Tarek El-Gaaly \*

tgaaly@cs.rutgers.edu

Ahmed Elgammal

elgammal@cs.rutgers.edu

Computer Science Department, Rutgers University

## Abstract

*This paper is focused on studying the view-manifold structure in the feature spaces implied by the different layers of Convolutional Neural Networks (CNN). There are several questions that this paper aims to answer: Does the learned CNN representation achieve viewpoint invariance? How does it achieve viewpoint invariance? Is it achieved by collapsing the view manifolds, or separating them while preserving them? At which layer is view invariance achieved? How can the structure of the view manifold at each layer of a deep convolutional neural network be quantified experimentally? How does fine-tuning of a pre-trained CNN on a multi-view dataset affect the representation at each layer of the network? In order to answer these questions we propose a methodology to quantify the deformation and degeneracy of view manifolds in CNN layers. We apply this methodology and report interesting results in this paper that answer the aforementioned questions.*

## 1. Introduction

Impressive results have been achieved recently with the application of Convolutional Neural Networks (CNNs) in the tasks of object categorizations [16] and detection [24, 9]. Several studies recently investigated different properties of the learned representations at different layers of the network, e.g. [26, 27, 3]. One fundamental question is how CNN models achieve different invariances. It is well understood that consecutive convolution and pooling layers can achieve translation invariant. Training CNN networks with a large dataset of images, with arbitrary viewpoints and arbitrary illumination, while optimizing the categorization loss helps to achieve viewpoint invariant and illumination invariant.

In this paper we focus on studying the viewpoint invariant properties of CNNs. In many applications, it is desired to estimate the pose of the object, for example for robot manipulation and scene understanding. Estimating pose and object categorization are tasks that contradict each other; estimating pose requires a representation capable of capturing the viewpoint variance, while viewpoint invariance is desired for categorization. Ultimately, the vision system should achieve a representation that can factor out the viewpoint for categorization and preserve viewpoint for pose estimation.

The biological vision system is able to recognize and categorize objects under wide variability in visual stimuli, and at the same time is able to recognize object pose. It is clear that images of the same object under different variability, in particular different views, lie on a low-dimensional manifold in the high-dimensional visual space defined by the retinal array ( $\sim 100$  million photoreceptors and  $\sim 1$  million retinal ganglion cells). DiCarlo and Cox [5] hypothesized that the ability of our brain to recognize objects, invariant to different viewing conditions, such as viewpoint, and at the same time estimate the pose, is fundamentally based on untangling the visual manifold encoded in neural population in the early vision areas (retinal ganglion cells, LGN, V1). They suggested that this is achieved through a series of successive transformation (re-representation) along the ventral stream (V1, V2, V4, to IT) that leads to an untangled population at IT. Despite this, it is unknown how the ventral stream achieves this untangling. They argued that since IT population supports tasks other than recognition, such as pose estimation, the manifold representation is some how "flattened" and "untangled" in the IT layer. DiCarlo and Cox's hypothesis is illustrated in Figure 1. They stress that the feedforward cascade of neural re-representation is a way to untangle the visual manifold.

Inspired by recent impressive results of CNNs and by DiCarlo and Cox's hypothesis [5] on manifold untangling,

\*Co-first author

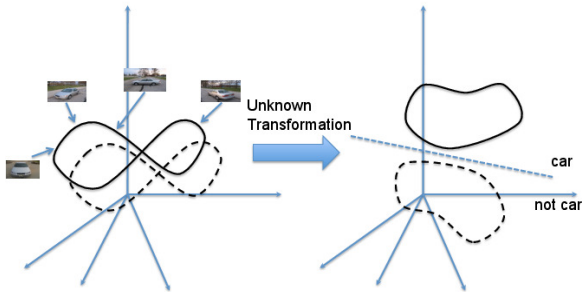


Figure 1: Illustration of DiCarlo and Cox model [5]: Left: tangled manifolds of different objects in early vision areas. Right: untangled (flattened) manifold representation in IT

this paper focuses on studying the view-manifold structure in the feature spaces implied by the different layers of CNNs. There are several questions that this paper aims to answer:

1. Does the learned CNN representations achieve viewpoint invariance? If so, how does it achieve viewpoint invariance? Is it by collapsing the view manifolds, or separating them while preserving them? At which layer is the view invariance achieved?
2. How to experimentally quantify the structure of the viewpoint manifold at each layer of a deep convolutional neural network?
3. How does fine-tuning of a pre-trained CNN, optimized for categorization on a multi-view dataset, affect the representation at each layer of the network?

In order to answer these questions, we present a methodology that helps to get an insight about the structure of the viewpoint manifold of different objects as well as the combined object-view manifold in the layers of CNN. We conducted a series of experiments to quantify the ability of different layers of a CNN to either preserve the view-manifold structure of data or achieve a view-invariant representation.

The contributions of the paper are as follows: (1) We propose a methodology to quantify and get insight into the manifold structures in the learned representation at different layers of CNNs. (2) We use this methodology to analyze the viewpoint manifold of pre-trained CNNs. (3) We study the effect of transfer learning a pre-trained network with two different objectives (optimizing category loss vs. optimizing pose loss) on the representation. (4) We draw important conclusions about the structure of the viewpoint-object manifold and how it coincides with DiCarlo and Cox’s hypothesis.

The paper begins by reviewing closely related work. Section 3 defines the problem, experimental setup, and the basic CNN network that our experiments are based upon.

Section 4 introduces our methodology of analysis. Sections 5 and 6 describe the findings on the pre-trained network and the fine-tuned networks respectively. The conclusion section summarizes our findings.

## 2. Related Work

LeCun *et al.* has widely used CNNs for various vision tasks [24, 15, 14, 20, 18]. The success of CNNs can be partially attributed to these efforts, in addition to training techniques that have been adopted. Krizhevsky *et al.* [16] used a CNN in the ImageNet Challenge 2012 and achieved state-of-the-art accuracy. Since then, there have been many variations in CNN architectures and learning techniques within different application contexts. In this section we mainly emphasize related works that focused on bringing an understanding of the representation learned at the different layers of CNNs and related architectures.

Yobinski *et al.* [26] studied how CNN layers transition from general to specific. An important finding in this study is that learning can be transferred, and by using fine-tuning, performance is boosted on novel data. Other transfer learning examples include [21, 6, 1]. Zeiler *et al.* [27] investigated the properties of CNN layers for the purpose of capturing object information. This study is built on the premise that there is no coherent understanding of why CNNs work well or how we can improve them. Interesting visualizations were used to explore the functions of layers and the in-trinsics of categorization. The study stated that CNN output layers are invariant to translation and scale but not to rotations. The study in [3] evaluated different deep architectures and compares between them. The effect of the output-layer dimensionality was explored.

## 3. Problem Definition and Experimental Setup

It is expected that multiple views of an object lie on intrinsically low-dimensional manifolds (*view manifold*<sup>1</sup>) in the input space. View manifolds of different instances and different objects are spread out in this input space, and therefore form jointly what we call the *object-view manifold*. The input space here denotes the  $R^{N \times M}$  space induced by an input image of size  $N \times M$ , which is analogous to the retinal array in the biological system. For the case of a viewing circle(s), the view manifold of each object instance is expected to be a 1-dimensional closed curve in the input space. The recovery of the category and pose of a test image reduces to finding which of the manifolds this image belongs to, and what is the intrinsic coordinate of that image within that manifold. This view of the problem is shared among manifold-based approaches such as [19, 28, 2]

<sup>1</sup>we use the terms *view manifold* and *viewpoint manifold* interchangeably

The ability of a vision system to recover the viewpoint is directly related to how the learned representation preserves the view manifold structure. If the transformation applied to the input space yields a representation that results in the collapsing of the view manifold, the system will no longer be able to discriminate between different views. Since each layer of a deep NN re-represents the input in a new feature space, the question would be how the re-representations deform a manifold that already exists in the input space. A deep NN would satisfy the hypothesis of “*flattening*” or “*untangling*” by DiCarlo and Cox [5], if the representation in a given layer separates the view manifolds of different instances, without collapsing them, in a way to be able to put a separating hyperplanes between different categories.

Typically CNN layers exhibit general-to-specific feature encoding, from Gabor-like features and color blobs at low layers to category-specific features at higher layers [27]. We can hypothesize that for the purpose of pose estimation, lower layers should hold more useful representations that might preserve the view manifold and be better for pose estimation. But which of these layers would be more useful, and where does the view-manifold collapse to view-invariance.

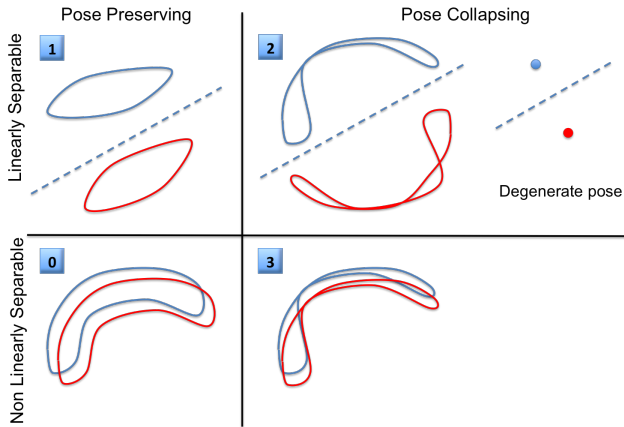


Figure 2: Sketches of four hypotheses about possible structures of the view manifolds of two objects in a given feature space

There are different hypotheses we can make about how the view manifolds of different objects are arranged in the feature space of a given layer. These hypotheses are shown in Figure 2. We arrange these hypotheses based on linear separability of the different objects’ view manifolds and the preservation of the view manifolds. Case 0 is the non-degenerate case where the visual manifolds preserve the pose information but are tangled and there is no linear separation between them (this might resemble the input space, similar to left case in Figure 1). Case 1 is the ultimate case where the view manifolds of different objects are preserved

by the transformation and are separable (similar to the right case in Figure 1). Case 2 is where the transformation in the network leads to separation of the object’s view manifold at the expense of collapsing these manifolds to achieve view invariance. Collapsing of the manifolds can be to different degrees, to the point where each object’s view manifold can be mapped to a single point. Case 3 is where the transformation results in more tangled manifolds (pose collapsing and non-separable). It is worth to notice that both cases 1 and 2 are view invariant representations. However, it is obvious that case 1 would be preferred since it also facilitates pose recovery. It is not obvious whether optimizing a network with a categorization loss result in case 1 or case 2. Getting an insight about which of these hypotheses are true in a given layer of a DNN is the goal of this paper. In Section 4 we propose a methodology to get us to that insight.

### 3.1. Experimental Settings

To get an insight into the representations of the different layers and answer the questions posed in Section 1 we experiment on two datasets: I) RGB-D dataset [17], II) Pascal3D+ dataset [25]. We selected the RGB-D dataset since it is the largest available multiview dataset with the most dense viewpoint sampling. The dataset contains 300 instances of tabletop objects (51 categories). Objects are set on a turntable and captured by an Xbox Kinect sensor (Kinect 2010) at 3 heights (30°, 45° and 60° elevation angles). The dense view sampling along each height is essential for our study to guarantee good sampling of the view manifold. We ignore the depth channel and only used the RGB channels.

Pascal3D+ is very challenging because it consists of images “in the wild”, in other words, images of object categories exhibiting high variability, captured in uncontrolled settings and under many different poses. Pascal3D+ contains 12 categories of rigid objects selected from the PASCAL VOC 2012 dataset [8]. These objects are annotated with 3D pose information (*i.e.* azimuth, elevation and distance to camera). Pascal3D+ also adds 3D annotated images of these 12 categories from the ImageNet dataset [4]. The *bottle* category is omitted in state-of-the-art results. This leaves 11 categories to experiment with. There are about 11,500 and 7,000 training images in ImageNet and Pascal3D+ subsets, respectively. For testing, there are about 11,200 and 6,900 testing images for ImageNet and Pascal3D+, respectively. On average there are about 3,000 object instances per category in Pascal3D+, making it a challenging dataset for estimating object pose.

The two datasets provide different aspect of the analysis. While the RGB-D provides dense sampling of each instance’s view manifold, Pascal3D+ dataset contains only very sparse sampling. Each instance is typically imaged from a single viewpoint, with multiple instances of the same

category sampling the view manifold at arbitrary points. Therefore, in our analysis we use the RGB-D dataset to analyze each instance viewpoint manifold and the combined object-viewpoint manifolds, while the Pascal3D provides analysis of the viewpoint manifold at the category level.

**Evaluation Split:** For our study, we need to make sure that the objects we are dealing with have non-degenerate view manifolds. We observed that many of the objects in the RGB-D dataset are ill-posed, in the sense that the poses of the object are not distinct. This happens when the objects have no discriminating texture or shape to be able to identify the different poses (e.g. a texture-less ball, apple or orange on a turntable). This will cause view manifold degeneracy. Therefore we select 34 out of the 51 categories as objects that possess pose variations across the viewpoints, and thus are not ill-posed with respect to pose estimation.

We split the data into training, validation and testing. Since in this datasets, most categories have few instances, we left out two random object instances per category, one for validation and one for testing. In the case where a category has less than 5 instances, we form the validation set for that category by randomly sampling from the training set. Besides the instance split, we also left out all the middle height for testing. Therefore, the testing set is composed of unseen instances and unseen heights and this allows us to more accurately evaluate the capability of the CNN architectures in discriminating categories and estimating pose of tabletop objects.

### 3.2. Base Network: Model0

The base network we use is the Convolutional Neural Network described in Krizhevsky *et al.* [16] and winner of LSVRC-2012 ImageNet challenge [23]. The CNN was composed of 8 layers (including 1000 neuron output layer corresponding to 1000 classes). We call these layers in order: Conv1, Pool1, Conv2, Pool2, Conv3, Conv4, Conv5, Pool5, FC6, FC7, FC8 where Pool indicates Max-Pooling layers, Conv indicates layers performing convolution on the previous layer and FC indicates fully connected layer. The last fully connected layer (FC8) is fed to a 1000-way softmax which produces a distribution over the category labels of the dataset.

## 4. Methodology

The goal of our methodology is two-folds: (1) study the transformation that happens to the viewpoint manifold of a specific object instance at different layers, (2) study the structure of the combined object-view manifold at each layer to get an insight about how tangled or untangled the different objects' viewpoint manifolds are. Both these approaches will get us an insight to which of the hypotheses explained in Section 3 is correct at each layer, at least relatively by comparing layers. This section introduces our

methodology, which consists of two sets of measurements to address the aforementioned two points. First, we introduce instance-specific measurements that quantify the viewpoint manifold in the different layers to help understand whether the layers preserve the manifold structure. *We performed extensive analysis on synthetic manifold data to validate the measures, which can be found in the appendix.* Second, we introduce empirical measurements that are designed to draw conclusions about the global object-viewpoint manifold (involving all instances).

### 4.1. Instance-Specific View Manifold Measurements

Let us denote the input data (images taken from a viewing circle and their pose labels) for of a specific object instance as  $\{(x_i \in \mathbb{R}^D, \theta_i \in [0, 2\pi]), i = 1 \dots N\}$ , where  $D$  denotes the dimensionality of the input image to the network, and  $N$  is the number of the images, which are equally spaced around the viewing circle. These images form the view manifold of that object in the input space denoted by  $\mathcal{M} = \{x_i\}_1^N$ . Applying each image to the network will result in a series of nonlinear transformations. Let us denote the transformation from the input to layer  $l$  by the function  $f_l(x) : \mathbb{R}^D \rightarrow \mathbb{R}^{d_l}$  where  $d_l$  is the dimensionality of the feature space of layer  $l$ . With an abuse of notation we also denote the transformation that happens to the manifold  $\mathcal{M}$  at layer  $l$  by  $\mathcal{M}^l = f_l(\mathcal{M}) = \{f_l(x_i)\}_1^N$ . After centering the data by subtracting the mean, let  $\mathbf{A}^l = [\hat{f}_l(x_1) \dots \hat{f}_l(x_N)]$  be the centered feature matrix at layer  $l$  of dimension  $d_l \times N$ , which corresponds to the centered transformed images of the given object. We call  $\mathbf{A}^l$  the sample matrix in layer  $l$ .

Since the dimensionality  $d_l$  of the feature space of each layer varies, we need to factor out the effect of the dimensionality. Since  $N \ll d_l$  the transformed images on all the layers lie on subspaces of dimension  $N$  in each of the feature spaces. Therefore we can change the bases to describe the samples using  $N$  dimensional subspace *i.e.*, we define the  $N \times N$  matrices  $\hat{\mathbf{A}}^l = \mathbf{U}^T \mathbf{A}^l$  where  $\mathbf{U} \in \mathbb{R}^{d_l \times N}$  are the orthonormal bases spanning the column space of  $\mathbf{A}^l$  (which we can get by SVD of  $\mathbf{A}^l = \mathbf{U}\mathbf{S}\mathbf{V}^T$ ). This projection just rotates the samples at each layer.

The following measures will be applied to the  $N$  transformed images, representing the view manifold of each object instance individually. To obtain an overall measures for each layer we will average these measures over all the object instances.

*1) Measure of spread - Nuclear Norm:* There are several possible measures of the spread of the data in the sample matrix of each view manifold. We use the nuclear norm (also known as the trace norm [13]) defined as  $\|\mathbf{A}\|_* = \text{Tr}(\sqrt{\mathbf{A}^T \mathbf{A}}) = \sum_{i=1}^N \sigma_i$ , *i.e.* it measure the sum of the singular values of  $\mathbf{A}$ .



2) *Subspace dimensionality measure - Effective-p*: As a measure of the effective dimensionality of the subspace where the view manifold lives, we define *Effective-p* as the minimum number of singular values (in decreasing order) that sum up to more than or equal to  $p\%$  of the nuclear norm,

$$\text{Effective} - p = \sup\{n : \sum_{i=1}^n \sigma_i / \sum_{i=1}^N \sigma_i \leq p/100\} \quad (1)$$

A smaller number means that the view manifold samples live in a lower dimensional subspace.

3) *Alignment Measure - KTA*: Ideally the view manifold resulting of the view sitting is a one-dimensional closed curve in the feature space, which can be thought as a deformed circle [28]. This manifold can be degenerate in the ultimate case to a single point in case of a textureless object. The goal of this measurement is to quantify how the transformed manifold locally preserves the original manifold structure. To this end we compare the kernel matrix of the transformed manifold at layer  $l$ , denote by  $\mathbf{K}_n^l$ , with the kernel matrix of the an embedding of the ideal view manifold on unit circle, denote by  $\mathbf{K}_n^\circ$ , where  $n$  indicates the local neighborhood size used in constructing the kernel matrix. We construct the neighborhood based on the pose labels.

Given these two kernel matrices we can define several convergence measures. We use *Kernel Target Alignment (KTA)* which has been used in the literature for kernel learning [12]. It simply finds a scale invariant dependency between two normalized kernel matrices<sup>2</sup>. Therefore, we define the alignment of the transformed view manifold  $\mathcal{M}^l$  at layer  $l$  with the ideal manifold as

$$KTA_n(\mathcal{M}^l) = \frac{\langle \mathbf{K}_n^l, \mathbf{K}_n^\circ \rangle_F}{\|\mathbf{K}_n^l\|_F \|\mathbf{K}_n^\circ\|_F} \quad (2)$$

4) *KPLS-regression measures*: Kernel Partial Least Squares (KPLS) [22] is a supervised regression method. KPLS iteratively extracts the set of principal components of the input kernel that are most correlated with the output<sup>3</sup>. We use KPLS to map from the transformed view manifold kernel  $\mathbf{K}_n^l$  (input kernel) to the unit circle kernel  $\mathbf{K}_n^\circ$  (output kernel). We enforce this mapping to use maximum of  $d = 5$  principal components, where  $d \ll N$  and  $N$  is the dimensionality of the kernels. Based on this mapping, we define *KPLS-Regression Error*, which measures the Normalized Cross Correlation between the output kernel and the

<sup>2</sup>We also experimented with HSIC [10], however HSIC is not scale invariant and is not designed to compare data in different feature spaces. Even after scaling the data, HSIC did not give any discriminative signal

<sup>3</sup>Unlike KPCA which extracts the principal components of the input kernel to maximize the variance of the output space, KPLS extracts the principal components of the input kernel that maximize the correlation with the output data.

mapped input kernel. This measures the mapping correctness from the transformed view manifold to the circle manifold kernel<sup>4</sup>.

5) *TPS-linearity measure*: In this measure we learn a regularized Thin Plate Spline (TPS) non-linear mapping [7] between the unit circle manifold and each  $\mathcal{M}^l$ . The reason for using TPS in particular is that the mapping has two parts, an affine part (linear polynomial) and a nonlinear part; details about the definition of the metric is in the appendix). Analysis of the two parts will tell us if the mapping is mostly linear or nonlinear. We use the *reciprocal-condition number (rcond)* of the sub coefficient matrices corresponding to the affine and the nonlinear part as a measure of the linearity of the transformation.

## 4.2. Global Object-Viewpoint Manifold Measures

To achieve an insight about the global arrangement of the different objects' view manifolds in a given feature space we suggest to use the following three empirical measurements:

6) *L-SVM*: For a test image  $x$  transformed to the  $l$ -th layer's feature space,  $f_l(x)$ , we compute the performance of a linear SVM classifier trained for categorization. Better performance of such a classifier directly implies more linear separability between different view manifolds of different categories.

7) *Kernel Pose Regression*: To evaluate whether the pose information is preserved in a local neighborhood of a point in a given feature space we evaluate the performance of kernel ridge regression for the task of pose estimation. Better performance implies better pose-preserving transformation, while poor performance indicates pose-collapsing transformation. The combination of L-SVM and kernel regression should be an indication to which of the hypotheses in Figure 2 is likely to be true.

8) *Local Neighborhood Analysis*: To evaluate the local manifold structure we also evaluate the performance of nearest neighbor classifiers for both category and pose estimation, with varying size of the neighborhood. This directly tell us whether the neighbors of a given point are from the same category and/or of similar poses. KNN for categorization cannot tell us about the linear separability of classes. However evaluating the pose estimation in a neighborhood of a datapoint gives us an insight about how the view manifolds are preserves, and even whether the view manifolds of different instances are aligned. To achieve this insight we use two different measurements:

1. KNN-Accuracy: the accuracy of KNN classifiers for category and pose estimation.

<sup>4</sup>We also used another KPLS measure we call *KPLS-Norm Ratio*, which can be found in the appendix

2. KNN-Gap: the drop in performance of each KNN classifier as the neighborhood size increases. In particular in our experiments we increase K from 1 to 9. Positive gap indicates a drop (expected) and negative gap indicates improvement in performance.

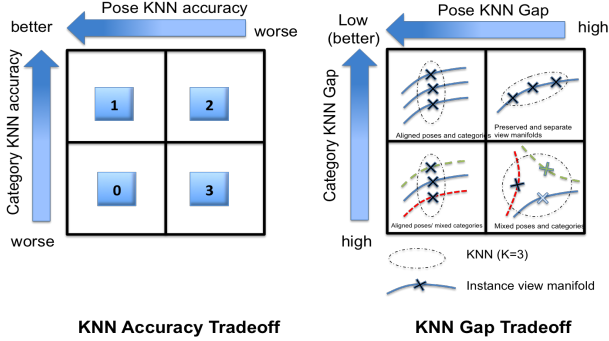


Figure 3: KNN Tradeoffs: Left) accuracy tradeoff between pose and category estimation using KNN. Right) Gap tradeoff (Gap is the drop in performance as K increases.)

The interaction between these two measures and how they tell us about the manifold structure is illustrated in Fig 3. The contrast between the accuracy of the KNN classifiers for pose and category directly implies which of the hypotheses in Figure 2 is likely. The analysis of KNN-Gap (assuming good 1-NN accuracy) gives further valuable information. As the KNN-gap reaches zero in both category and pose KNN classifiers, this implies that neighborhoods are from the same category and has the same pose, which indicates that the representation aligns the view manifolds of different instances of the same category. If the view manifolds of such instances are preserved and separated in the space, and the neighbors of a given point are from the same instance, this would imply small gap in the category KNN classifier and bigger gap in pose KNN classifier. Low gap in pose KNN vs high gap in category CNN implies the representation aligns view manifolds of instances of different categories. A high gap in both obviously implies the representation is tangling the manifolds such that a small neighborhood contains points from different categories and different poses. Notice that this implications are only valid when the 1-NN accuracy is high.

## 5. Analysis of the Pre-trained Network

### 5.1. Instance View Manifold Analysis

Figure 4 shows the application of the instance-specific view manifold measurements on the images of the RGBD dataset when applied to a pre-trained network (Model0 - no fine-tuning). This gives us an insight on the transformation that happens to the view manifold of each object instance

at each layer of the network. Figure 4a shows that the nuclear norm of the transformed view manifolds in Model0 is almost monotonically decreasing as we go higher in the network, which indicates that the view manifolds is more spread in the lower layers. In fact at the output layer of Model0 the nuclear norm becomes too small, which indicates that the view manifold is collapsing to reach view invariant representation at this layer. Figure 4b ( $p = 90\%$ ) shows that subspace dimension varies within a small range in the lower layers and it reduces dramatically in fully connected layers, which indicates that the network tries to achieve view invariance. The minimum is achieved at FC8 (even without fine tuning). Figure 4c shows the KTA applied to Model0, where we can notice that the alignment is almost similar across the lower layers, with Pool5 having the maximum alignment, and then starts to drop at the very high layers. which indicates that after Pool5, the FC layers try to achieve view invariant. Fig 4d shows that KPLS regression error on Model0 dramatically reduces from FC8 down to Pool5, where Pool5 has the least error. In general the lower layers have less error. This indicates that the lower layers preserve higher correlation with the ideal manifold structure. Fig 4e shows that the mapping is highly linear, which is expected because of the high dimensionality of the feature spaces. From Fig 4e we can clearly notice that the lower layers has more better-conditioned linear mapping<sup>5</sup>.

From these measurements we can conclude: (1) The lower layers preserve the view manifolds. The manifolds start to collapse in the FC layers to achieve view invariance. Preserving the view manifold at the lower layers is intuitive because of the nature of the convolutional layers. (2) The manifold at Pool5 achieves the best alignment with the pose labels. This is a less intuitive result; why does the representation after successive convolutions and pooling improves the view manifold alignment? even without seeing any dense view manifold in training, and even without any pose labels being involved in the loss. The hypotheses we have to justify that Pool5 has better alignment than the lower layers is that Pool5 has better translation invariant properties, which results in improvement of the view manifold alignment.

### 5.2. Global Object-View Manifold Analysis

The performance of Linear SVM and Kernel Regression is shown in Figure 5, using RGBD dataset (plots for Pascal3D are in the appendix). The figure clearly shows the conflict in the representation of the pre-trained network (categorization increases and pose estimation decreases). Linear separability of category is almost monotonically increasing up to FC6. Linear separability in FC7 and FC8 is worse, which is expected as they are task specific (no

<sup>5</sup>Figures for the nonlinear part can be seen in the appendix, which shows very small values ( $\approx 10^{-11}$ ) compared to the linear part

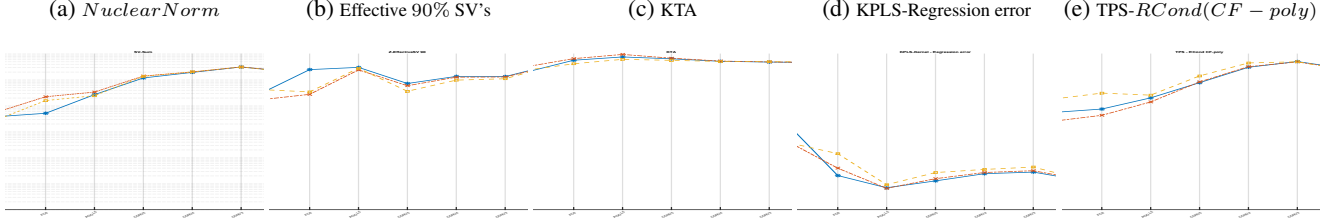


Figure 4: Measurement analysis for the view-manifold in RGBD dataset based on features extracted from different layers of several CNN models. Every figure shows single measurement. Multiple lines is for different CNN model. X-axis is labeled by the layers. Larger versions of the figures are available in the appendix.

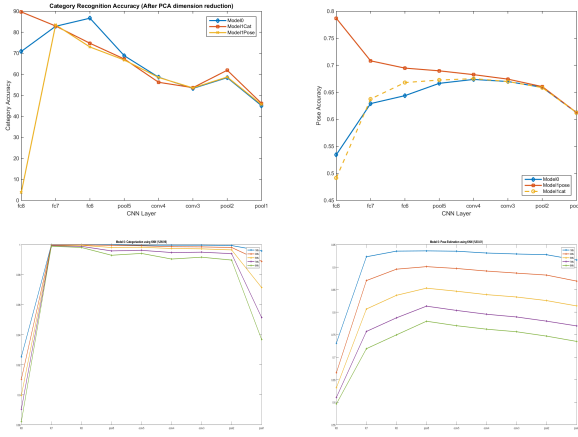


Figure 5: Top-Left: the performance of linear SVM category classification over the layers of different model. Top-Right: the performance of pose regression over the layers of different models. Bottom-Left: KNN categorization. Bottom-right: KNN pose estimation.

fine-tuning). Surprisingly Pool1 features perform very bad, despite being the most general features (typically they show Gabor like features and color blobs). In contrast, for pose estimation, the performance increases as we go lower in the network up to Conv4 and then slightly decreases. This confirms our hypothesis that lower layers offer better feature encoding for pose estimation. It seems that Pool5 provides feature encoding that offer the best compromise in performance, which indicates that it is the best in compromising between the linear separation of categories and the preservation of the view-manifold structure.

What is surprising is that the pose estimation results do not drop dramatically in FC6 and FC7. We can still estimate the pose (with accuracy around 63%) from the representation at these layers, even without any training on pose labels. This highly suggests that the network preserves the view manifold structure to some degree. For examples taking the accuracy as probability at layer FC6, we can vaguely conclude that 90% of the manifolds are linearly separable

Approach	Split	Categorization %	Pose (AAAI metric)
Model0 (SVM/Kernel Regression) on FC6	1	86.71	64.39
Model0 (SVM/Kernel Regression) on conv4	1	58.64	67.39
HOG (SVM/Kernel Regression)	1	80.26	27.95
Model1	1	89.63	81.21%, 69.58 (< 22.5), 81.09 (< 45)

Table 1: RGBD Dataset Results for Model1, Model0, and HOG

and 65% are pose preserved (we are somewhere between hypotheses 1 and 2 at this layer).

The aforementioned conclusion is also confirmed by the KNN analysis. Very high accuracy is achieved using KNN for category and pose. The category gap is reducing as we go up in the network up to FC7 (almost 0 gap at FC6 and FC7). In contrast the gap is large at all layers for pose estimation. This indicates separation of the instances' view manifolds where the individual manifolds are not collapsed (This is why as we increase the neighborhood, the category performance stays the same while pose estimation decreases smoothly - See the top-right block of Figure 3-right for illustration). The results above consistently imply that the higher layers of CNN (except FC8 which is task specific), even without any fine-tuning on the dataset, and even without any pose label optimization achieve representations that separate and highly preserve the view manifold structure.

Tables 1 and 2 show the quantitative results of our models, compared to baselines, on the RGBD Dataset and Pascal3D+. Table 2 shows our quantitative results compared against two previous methods [29] and [25], using the two metrics  $< 45^\circ$  and  $< 22.5^\circ$ . It is important to note that the comparison with [25] is unfair because they solve for detection and pose simultaneously while we do not solve for detection. We solve for categorization and pose.

Approach	Categorization %	Pose (AAAI metric)
<i>Model0 (SVM/Kernel Regression)</i>		
FC6	73.64	49.72
FC7	76.38	48.24
FC8	71.13	45.41
<i>Model1 (SVM/Kernel Regression)</i>		
FC6	74.65	54.41
FC7	79.25	54.07
FC8	84.12	60.31
<i>Model0 NN</i>		
FC6	60.05	61.11
FC7	69.89	61.38
FC8	61.26	60.32
<i>Model1 NN</i>		
FC6	73.50	65.87
FC7	77.30	66.07
FC8	83.07	70.54
<i>Model1 (direct prediction from CNN)</i>		
output	84.00	71.60 (AAAI), 47.34(<22.5), 61.30 (<45)
<i>State of the Art Methods</i>		
[29]	-	44.20 (< 22.5), 59.00 (<45)
[25]	-	15.6% (<22.5), 18.7% (<45)

Table 2: Pascal3D Performance. Here we see our results compared to the two baselines from [29] and [25] using the two metrics  $< 45^\circ$  and  $< 22.5^\circ$ . It is important to note that the comparison with [25] is slightly unfair because they solve for detection and pose simultaneously while we do not solve for detection. We solve for categorization and pose. Model1 here outperforms both [29] and [25] (despite the unfair comparison with the latter approach).

## 6. Effect of Transfer Learning

In order to study the effect of fine-tuning the network (transfer learning to a new dataset) on the representation we trained the following model (denoted as Model1). This architecture consists of two parallel CNNs: one with category output nodes (Model1-Cat), and one with binned pose output nodes (Model1-Pose). We used 34 and 11 category nodes for RGBD and Pascal3D datasets respectively; while we used 16 pose nodes for both datasets). The parameters of both CNNs were initialized by Model0 parameters up to FC7. The parameters connecting FC7 to the output nodes are randomly initialized on both networks and they are fine-tuned by minimizing the categorization loss for Model1-Cat and the pose loss for Model1-pose. The purpose of these architectures is to study the effect of fine-tuning when the category and pose are independently optimized.

We applied all the measures described in Sec 4 to understand how the view manifolds will be affected after such tuning. The questions are: To what degree optimizing on category should damage the ability of the network to encode view manifolds. On the other hand, how optimizing on pose should enhance that ability. Model1-Cat indicates the effect of optimizing on category, while Model1-Pose indicates the effect of optimizing on pose.

Fig 4 shows the five view manifold measures for the different layers of Model1(Cat/Pose), in comparison with Model0. In terms of data spread, from Fig 4a shows that

the spread at FC8 has doubled after fine tuning on pose (Model1-Pose). Fig 4b shows the fine tuning on category (Model1-Cat) caused the view manifold subspace dimensionality to significantly reduce to 1, where it became totally view invariant. Optimizing on pose slightly enlarged the subspace dimensionality (*i.e.* become better) at FC8 and FC7. Fig 4c clearly shows the significant improvement achieved by fine tuning on pose, where the alignment of FC8 jumped to close to 0.9 from about 0.78, while fine tuning on category reduces the alignment of FC8 to close to 0.65. Similar behavior is also apparent in the KPLS ratio for FC8 and FC7 (sup-mat).

One very surprising result is that optimizing on pose makes the pose KTA alignment worse at the lower layers, while optimizing on category makes the pose alignment better compared to model0. In fact, although optimizing on pose significantly helps aligning FC8 with pose labels, Pool5 still achieves the best KTA alignment and the least regression reconstruction error. The regression reconstruction error in Fig 4d clearly shows significant improvement in the representation of FC8 and FC7 to preserve the view manifold. One surprising finding from these plots is that the representation of FC6 becomes worse after fine tuning for both pose and category. Fig 4e indicates that the deformation of the view manifold is reduced as a result of fine tuning on pose (larger rcond number), while it increases as a result of fine tuning on category.

On the global object-view manifold structure, we notice from Figures 5 some intuitive behavior at FC8. Basically optimizing on pose reduces the linear separability and increases the view manifold preservation (moves the representation towards hypothesis 0). In contrast, optimizing the category significantly improves the linear separability at FC9, however, interestingly, it only slightly reduces the pose estimation performance to be slightly less than 50%. Combining this conclusion with the observation from Fig 4b, that the view manifold subspace dimensionality reduces to 1, this implies that optimizing on category collapses the view manifolds to a line, but they are not totally degenerate. What is less obvious is the effect of fine tuning on the lower layers than FC8. Surprisingly, optimizing on pose did not affect the linear separability of FC7. Another very interesting observation is that optimizing on category actually improves the pose estimation slightly at the FC7, FC6, and Pool5; and did not reduce it at lower layers. This implies that fine tuning by optimizing on category only improved the internal view manifold preservation at the network, even without any pose labels. Analysis using KNN measures, as well as results of fine-tuning on Pascal3D dataset are available in the appendix.



## 7. Conclusions

In this paper we present an in-depth analysis and discussion of the view-invariant properties of CNNs. We proposed a methodology to analyze individual instance's view manifolds, as well as the global object-view manifold. We applied the methodology on a pre-trained CNN, as well as two fine-tuned CNNs, one optimized for category and one for pose. We performed the analysis based on two multi-view datasets (RGBD and Pascal3D+). Due to the limited space, we mainly show the plots of the RGBD dataset in the main paper, while the plots for the Pascal3D+ can be seen in the appendix. Applications on both datasets give consistent conclusions.

Based on the proposed methodology and the datasets, we analyzed the layers of the pre-trained and fine-tuned CNNs. There are several findings from our analysis that are detailed throughout the paper, some of them are intuitive and some are surprising. We find that a pre-trained network captures representations that highly preserve the manifold structure at most of the network layers, including the fully connected layers, except the final layer. Although the model is pre-trained on ImageNet, not a densely sampled multi-view dataset, still, the layers have the capacity to encode view manifold structure. It is clear from the analysis that, except of the last layer, the representation tries to achieve view invariance by separating individual instances' view manifolds while preserving them, instead of collapsing the view manifolds to degenerate representations. This is violated at the last layer which enforces view invariance.

*Overall, our analysis using linear SVM, kernel regression, KNN, combined with the manifold analysis, makes us believe that CNN is a model that simulate the manifold flattening hypothesis of Cox and DiCarlo [5] even without training on multi-view dataset and without involving pose labels in the objective's loss.*

Another interesting finding is that Pool 5 offers a feature space where the manifold structure is still preserved to the best degree. Pool 5 shows better representation for the view-manifold than early layers like Pool1. We hypothesize that this is because Pool5 has better translation and rotation invariant properties, which enhance the representation of the view manifold encoding.

We also showed the effect of fine-tuning the network on multi-view datasets, which can achieve very good pose estimation performance. In this paper we only studied the effect of independent pose and category loss optimization. Optimizing on category achieves view invariance at the very last fully connected layers; interestingly it enhances the view-point preservation at earlier layers. We also find that fine-tuning mainly affects the higher layers and rarely affects the lower layers.

In this work our goal is not to propose any new architecture or algorithm to compete with the state of the art in

pose estimation. However, it is clear that if we compare the results we achieve by fine tuning the network on pose and category independently we can achieve better results than what is generally reported in the literature. We keep these results to the appendix as a guide to the reviewers, without distracting the reader from our main goal.

## References

- [1] P. Agrawal, R. Girshick, and J. Malik. Analyzing the performance of multilayer neural networks for object recognition. In *Computer Vision—ECCV 2014*, pages 329–344. Springer, 2014. 2
- [2] A. Bakry and A. Elgammal. Untangling object-view manifold for multiview recognition and pose estimation. *ECCV*, 2014. 2
- [3] K. Chatfield, K. Simonyan, A. Vedaldi, and A. Zisserman. Return of the devil in the details: Delving deep into convolutional nets. *CoRR*, abs/1405.3531, 2014. 1, 2
- [4] J. Deng, W. Dong, R. Socher, L.-J. Li, K. Li, and L. Fei-Fei. Imagenet: A large-scale hierarchical image database. In *CVPR*, 2009. 3
- [5] J. J. DiCarlo and D. D. Cox. Untangling invariant object recognition. *Trends in cognitive sciences*, 11(8):333–341, 2007. 1, 2, 3, 9
- [6] J. Donahue, Y. Jia, O. Vinyals, J. Hoffman, N. Zhang, E. Tzeng, and T. Darrell. Decaf: A deep convolutional activation feature for generic visual recognition. *arXiv preprint arXiv:1310.1531*, 2013. 2
- [7] J. Duchon. Splines minimizing rotation-invariant seminorms in sobolev spaces. In *Constructive theory of functions of several variables*, pages 85–100. Springer, 1977. 5, 16
- [8] M. Everingham, L. V. Gool, C. K. I. Williams, J. Winn, and A. Zisserman. The pascal visual object classes (VOC) challenge. *International Journal of Computer Vision (IJCV)*, 2010. 3
- [9] R. B. Girshick, J. Donahue, T. Darrell, and J. Malik. Rich feature hierarchies for accurate object detection and semantic segmentation. *CoRR*, abs/1311.2524, 2013. 1
- [10] A. Gretton, O. Bousquet, A. Smola, and B. Schölkopf. Measuring statistical dependence with hilbert-schmidt norms. In *Algorithmic learning theory*, pages 63–77. Springer, 2005. 5
- [11] A. Gretton, O. Bousquet, A. Smola, and B. Schölkopf. Measuring statistical dependence with hilbert-schmidt norms. In *Proceedings of the 16th International Conference on Algorithmic Learning Theory, ALT'05*, pages 63–77, Berlin, Heidelberg, 2005. Springer-Verlag. 13
- [12] D. H. B. CJC, K. L. S. A., and V. V. Support vector regression machines. *Advances in Neural Information Processing Systems*, 1996. 5
- [13] R. A. Horn. *Matrix Analysis*. 4
- [14] K. Jarrett, K. Kavukcuoglu, and Y. Lecun. What is the best multi-stage architecture for object recognition?, 2009. 2
- [15] K. Kavukcuoglu, P. Sermanet, Y.-L. Boureau, K. Gregor, M. Mathieu, and Y. LeCun. Learning convolutional feature hierarchies for visual recognition. In J. D. Lafferty, C. K. I.

Williams, J. Shawe-Taylor, R. S. Zemel, and A. Culotta, editors, *NIPS*, pages 1090–1098. Curran Associates, Inc., 2010.

2

- [16] A. Krizhevsky, I. Sutskever, and G. Hinton. Imagenet classification with deep convolutional neural networks. In *Advances in Neural Information Processing Systems 25*, pages 1106–1114, 2012. 1, 2, 4
- [17] K. Lai, L. Bo, X. Ren, and D. Fox. A large-scale hierarchical multi-view rgb-d object dataset. In *Robotics and Automation (ICRA), 2011 IEEE International Conference on*, pages 1817–1824. IEEE, 2011. 3
- [18] Y. LeCun, F. J. Huang, and L. Bottou. Learning methods for generic object recognition with invariance to pose and lighting. In *Proceedings of the 2004 IEEE Computer Society Conference on Computer Vision and Pattern Recognition*, CVPR’04, pages 97–104, Washington, DC, USA, 2004. IEEE Computer Society. 2
- [19] H. Murase and S. Nayar. Visual learning and recognition of 3d objects from appearance. *International Journal of Computer Vision*, 14:5–24, 1995. 2
- [20] M. Ranzato, F. Huang, Y. Boureau, and Y. LeCun. Unsupervised learning of invariant feature hierarchies with applications to object recognition. In *Proc. Computer Vision and Pattern Recognition Conference (CVPR’07)*. IEEE Press, 2007. 2
- [21] A. S. Razavian, H. Azizpour, J. Sullivan, and S. Carlsson. Cnn features off-the-shelf: an astounding baseline for recognition. In *Computer Vision and Pattern Recognition Workshops (CVPRW), 2014 IEEE Conference on*, pages 512–519. IEEE, 2014. 2
- [22] R. Rosipal and L. J. Trejo. Kernel partial least squares regression in reproducing kernel hilbert space. *J. Mach. Learn. Res.*, 2:97–123, Mar. 2002. 5, 14
- [23] O. Russakovsky, J. Deng, H. Su, J. Krause, S. Satheesh, S. Ma, Z. Huang, A. Karpathy, A. Khosla, M. S. Bernstein, A. C. Berg, and L. Fei-Fei. Imagenet large scale visual recognition challenge. *CoRR*, abs/1409.0575, 2014. 4
- [24] P. Sermanet, D. Eigen, X. Zhang, M. Mathieu, R. Fergus, and Y. LeCun. Overfeat: Integrated recognition, localization and detection using convolutional networks. *CoRR*, abs/1312.6229, 2013. 1, 2
- [25] Y. Xiang, R. Mottaghi, and S. Savarese. Beyond pascal: A benchmark for 3d object detection in the wild. In *IEEE Winter Conference on Applications of Computer Vision (WACV)*, 2014. 3, 7, 8
- [26] J. Yosinski, J. Clune, Y. Bengio, and H. Lipson. How transferable are features in deep neural networks? *ArXiv e-prints*, Nov. 2014. 1, 2
- [27] M. D. Zeiler and R. Fergus. Visualizing and understanding convolutional networks. *CoRR*, abs/1311.2901, 2013. 1, 2, 3
- [28] H. Zhang, T. El-Gaaly, and A. Elgammal. Joint object and pose recognition using homeomorphic manifold analysis. *AAAI*, 2013. 2, 5
- [29] H. Zhang, T. El-Gaaly, A. Elgammal, and Z. Jiang. Factorization of view-object manifolds for joint object recognition and pose estimation. *arXiv preprint arXiv:1503.06813*, 2015. 7, 8

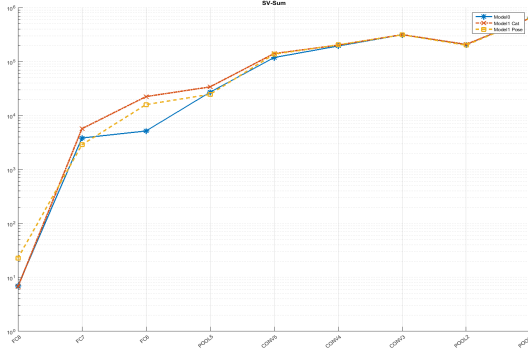
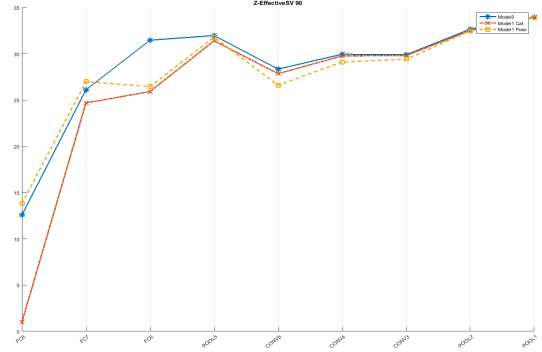
Figure 6: *NuclearNorm*

Figure 7: Effective 90% SV's



## Appendix

### A. Pose and Categorization Performance on RGBD and Pascal3D datasets

The two metrics  $< 22.5$  and  $< 45$  are the percentages of test samples that satisfy  $AE < 22.5^\circ$  and  $AE < 45^\circ$ , respectively where the Absolute Error (AE) is  $AE = |EstimatedAngle - GroundTruth|$ . The AAAI pose metric is defined as

$$\Delta(\theta_i, \theta_j) = \min(|\theta_i - \theta_j|, 2\pi - |\theta_i - \theta_j|) / \pi \quad (3)$$

### B. Larger Versions of Figure 4

Figures 6 through 10 show larger figures of the measurement analysis for the view-manifold on the images of the RGBD dataset. These are based on features extracted from different layers of several CNN models. Every figure shows single measurements. Multiple lines are for different CNN models. The X-axis is labeled by the layers.

### C. Synthetic Data Analysis

In this work, we have explored many different measurements and filter them out to use only those that expose the correct properties of the view-manifolds. Besides the intuitive reasoning that we provided for choosing the measurements, in this section, we show empirical results to quantify efficiency of the chosen measurements.

To this end, we synthesized a set of well designed view-manifolds. Analyzing these manifolds is intended to identify the robust and informative set of measurements to be used in further analysis. To be qualified for comparing different manifolds, the synthesized manifolds is designed to encode interesting properties of any view-manifold such as:

- Dimensionality (of the Euclidean space where the manifold lives)
- Sparsity of the manifold

Figure 8: KTA

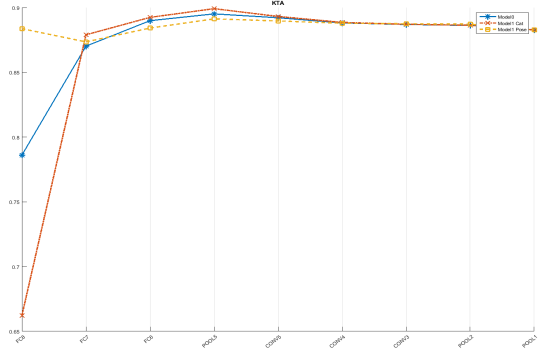


Figure 9: KPLS-Regression error

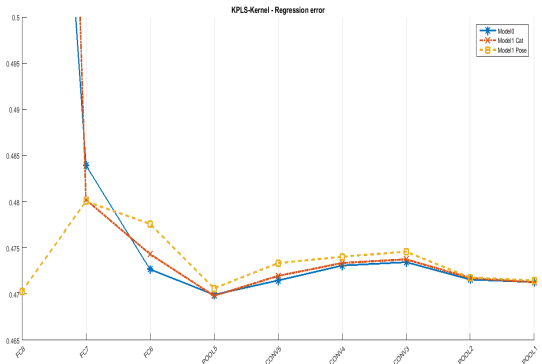
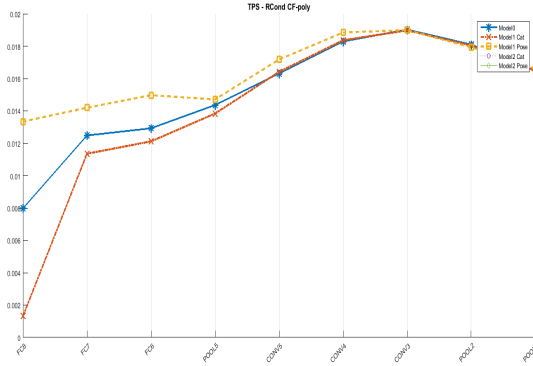


Figure 10: TPS- $RCond(CF - poly)$



- Smoothness of the manifold
- Deformation of the manifold w.r.t the *view-circle*
- Variance of data-points

Recall, The view-circle is a view-manifold, where all the viewpoints form a perfect circle and the object is assumed to be located at the center of this circle.

In the rest of this section, we list detailed description of the synthetic manifolds. Then, we use them to analyze the selected measurements.

## D. Dataset Description

The manifolds in this dataset can be categories as:

- Circle Orthogonally projected to high-dimensional subspaces (Manifold sets 1 and 2)
- Unit circle projected to a nonlinear surface (manifold 3)
- Unit circle projected to 3D-Sphere with radius  $r$  ( $S_2^r$ ) (sets 4 and 5)
- Nonlinear smooth curve projected on  $S_2^r$  (set 6)
- Discontinuous smooth curve projected on  $S_2^r$  (set 7)
- Random manifolds (sets 8 and 9)
- Collapsed manifolds in a single point or very small region (set 10).

The manifolds are described using the dimensionality ( $d$ ), sparsity ( $s = \frac{n}{d}$ ) and  $n$ , the number of points representing the view-manifold, smoothness, deformation w.r.t the view-circle.

Let the view-manifold be parameterized by the single dimensional variable. Let  $S$  is the two dimensional representation of the unit circle.  $S = \{(\cos(t), \sin(t)) | t =$

$\{0, \frac{2\pi}{n}, \frac{4\pi}{n}, \dots, \frac{2(n-1)\pi}{n}\}\}$ . For each view-manifold ( $\mathcal{M}$ ), we generated  $n$  points in a  $d$ -Dim space.

### • Perfect view-circle in high-dimensional space

- Manifold 1:  $n = 100$ ,  $d \in \{10, 300, 600, 900, 1200, 1500, 1800\}$ , therefore, the sparsity varies from very dense ( $s = 10$ ) to very sparse ( $s = 1/20$ )
- Manifold 2:  $d = 500$ ,  $n \in \{50, 150, 250, 350, 450, 550, 650, 750\}$ , therefore, the manifold varies from very sparse ( $s = 1/10$ ) to dense ( $s = 1.5$ )

- **View-circle projected nonlinearly to Sinusoidal Surface.** The manifold has  $n = 100$  points and live in  $d = 3$ -Dim space, so it is very dense  $s = 33.33$  To project the view-circle on this surface we follow these steps:

- Let  $f_n$  be the projection function on the surface,

$$f_n(x, y) = \sin(3x)\cos(2y)^2$$

- The projected manifold  $Z$  is defined by

$$Z = \{(x, y, f_n(x, y)) | (x, y) \in S\}$$

- Manifold 3 represents this type of manifolds in our dataset.

- **Dense view-circle projected nonlinearly to  $S_2^r$ , with  $r \in \{1, 50, 100, 150\}$ ,  $d = 3$ ,  $n = 100$  ( $s = 33.33$ )**

To project the view-circle on  $S_2^r$ , we use the following projection function

$$f(\theta, \phi) = (\sin(\phi)\cos(\theta), \sin(\phi)\sin(\theta), \cos(\phi))$$

Where

$$\theta \in \{0, \frac{2\pi}{n}, \frac{4\pi}{n}, \dots, \frac{2(n-1)\pi}{n}\}$$

- Manifold 4: Slightly deformed manifold, Figure 11b

$$\phi = \frac{\pi}{4}\sin(\theta) + \frac{\pi}{2}; \forall \theta$$

- Manifold 5: Slightly deformed manifold with added Gaussian noise with  $\mu = 0$  mean  $\sigma = 0.01$ .  $\theta$  and  $\phi$  as in Manifold 4.

- Manifold 6: Highly deformed manifold, Figure 11c

$$\phi = \frac{\pi}{4}\sin(5\theta) + \frac{\pi}{2}; \forall \theta$$



- Manifold 7: Highly deformed and broken/discontinuous manifold.

$$\phi = \frac{\pi}{4} \tan(0.75\theta) + \frac{\pi}{2}; \forall \theta$$

- **Random manifold with independent dimensions**

- Manifold 8: Uniform random points with  $d \in \{10, 100, 500, 1000, 4000\}$ ,  $n = 100$ , therefore, the sparsity varies from very dense ( $s = 10$ ) to very sparse ( $s = 1/100$ )
- Manifold 9: Normal random points has been generated with  $d = 100$ ,  $n \in \{20, 40, \dots, 200\}$ , therefore, sparsity varies from very sparse ( $s = 1/10$ ) to dense ( $s = 2$ )

- **Collapsed Manifold with random noise**

- Manifold 10: Portion of the points ( $m = n/4$ ), in this manifold, have been generated by Gaussian Random with  $\mu = 0$ ,  $\sigma = 0.01$ , therefore, the rest are a copied version of this portion  $d \in \{10, 100, 500, 1000, 4000\}$ ,  $n = 100$

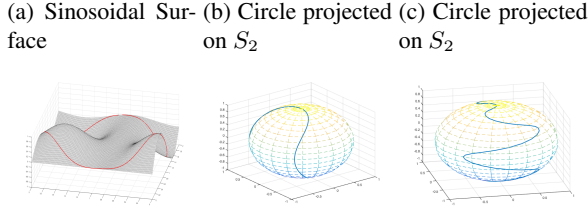


Figure 11: Manifold Visualization

## E. Analysis

Recall, the objective of using the synthetic data is to verify the efficiency of selected measurements. Figure 12 shows the results of applying the measurements to the synthetic-data. Figure 12a shows the Nuclear Norm (defined in the main paper) for all manifolds. This figure shows the variability between the manifolds in the variance. For the set of manifolds 4-7, projecting the view-circle onto sphere with different sizes affects the variance of the points. Encoding different Nuclear Norm is subjected to discover the measurements that are sensitive to the data variance.

From Figure 12b, defined in the main paper, we can see the effective dimensions for each manifold. Manifolds 1 and 2 have two effective dimensions. Manifolds 3-7 has three effective dimensions. Since the points in Manifolds 8-10 are generated randomly so they have maximum rank.

The kernel alignment measures: KTA (Figure 12c) and HSIC (Figure 12d) measure the correlation between the

view-manifold and the view-circle. These two figures show significant better alignment of the view-manifold of sets 1-6 than the alignment of the random manifolds. Since Hilbert-Schmidt Independence Criterion (HSIC) [11] does not add any information more than KTA. We select the KTA measurement because it exposes absolute alignment confidence for the manifolds 1 and 2.

KPLS-regression Error is shown in Figure 12e. Dispite the vast variability of variance and dimensionality, this measure is consistent and gives small value for all smooth manifold. This measure can also detect the collapsing manifolds, since it gives very large error value.

As we mentioned in Section G, that using both measurements KPLS-Regression Error and KPLS-Norm Ratio gives more robust conclusion about the manifold. Fig 12f shows a clear trend, since it gives significant high values for random manifolds. This is because, the subspace of the random points covers the entire space. When  $\frac{norm(G_d)}{norm(G_0)} \equiv 1$ , this means that the first  $d$  components extracted from  $G_0$  are far from being principal. If they are principal components, they would change the energy of the matrix  $G$  significantly. On the other side, the Effective dimensionality of the smooth manifolds 1-6 is  $D \leq 3$ , which make the limit  $d > D$ . That is why the ratio  $\frac{norm(G_d)}{norm(G_0)} \ll 1$  because we have extracted all the principal components of those manifolds. That is why KPLS-Regression Error for these manifolds is very small.

As mentioned in the main paper, TPS-linearity measure ( $TPS - RCond(CF - Poly)$ ) scores on the stability of the polynomial mapping from the points on the view-circle and the points on the view-manifold. Fig 12g shows perfect scoring for Manifolds 1 and 2. Combining this figure with Fig 12h gives a complete impression about the mapping stability (Polynomial and Non-Polynomial). However, the range of the values of TPS-nonlinearity measure ( $TPS - RCond(CF - nonPoly)$ ) is in  $BigO(10^{-8})$ , which decrease its robustness.

## F. Analysis using KNN Measure

In this section we show KNN performance for Model1Cat and Model1Pose on the RGBD dataset for both pose estimation and categorization tasks (4 figures from Figure 13 to 16). We also analyze the performance of Model0, Model1Pose and Model1Cat on Pascal3D+ for both pose estimation and categorization tasks (6 figures from Figure 17 to 22).

## G. KPLS-Norm Ratio and TPS (More Measurements)

We define and show the results of more measurements such as KPLS-Norm Ratio and TPS-nonPolynomial. We use here the same notations and definitions stated in Section 4 in the main paper.

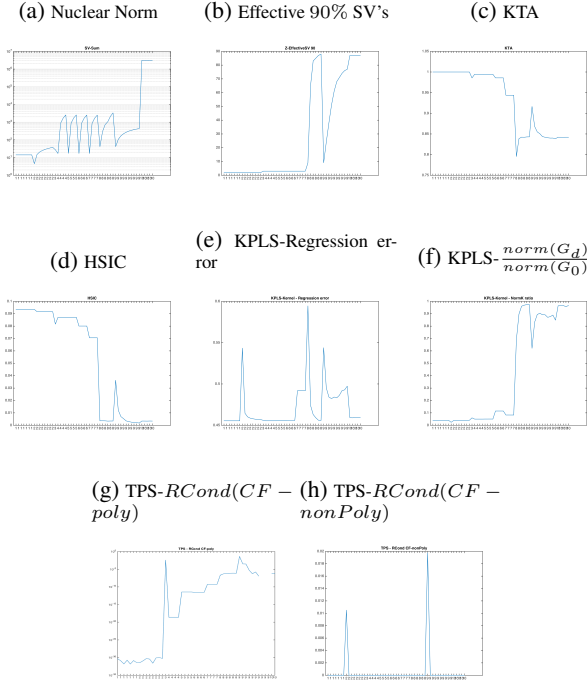


Figure 12: Measurement analysis for the synthetic manifolds. Every figure shows single measurement. X-axis is labeled by the manifold category number.

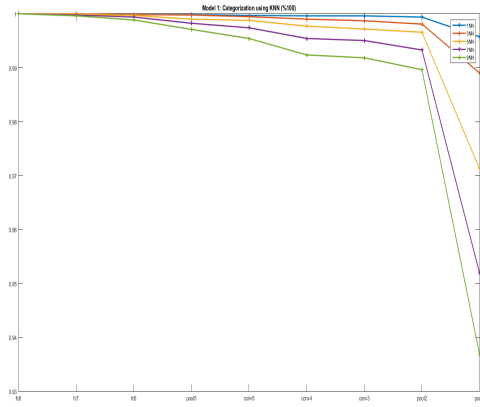


Figure 13: RGBD Dataset: Model1Cat KNN performance on Categorization Task

1) *KPLS-Norm Ratio*: Kernel Partial Least Squares (KPLS) [22] is a supervised regression method. KPLS iteratively extracts a set of principal components of the input kernel that are most correlated with the output. While KPCA extracts the principal components (PCs) of the kernel of the input data to maximize the variance of the output space, KPLS extracts the PCs of the kernel of the input data that

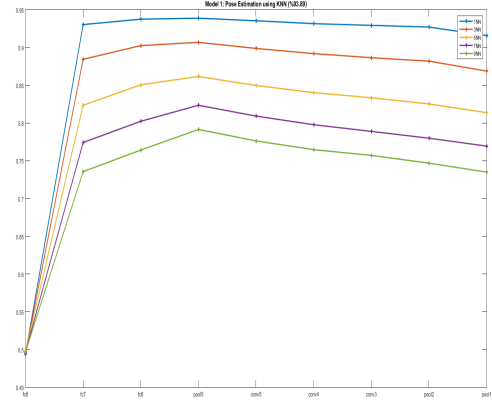


Figure 14: RGBD Dataset: Model1Cat KNN performance on Pose Estimation Task

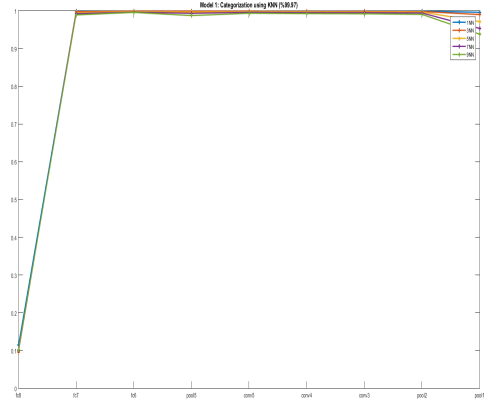


Figure 15: RGBD Dataset: Model1Pose KNN performance on Categorization Task

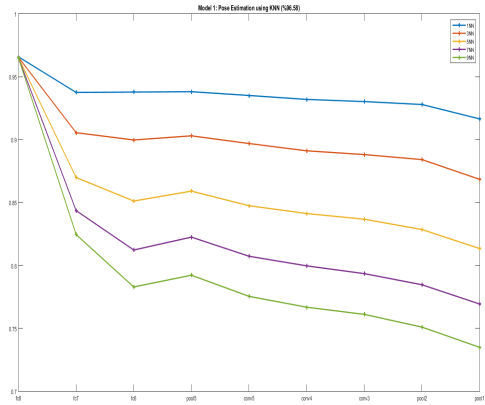


Figure 16: RGBD Dataset: Model1Pose KNN performance on Pose Estimation Task

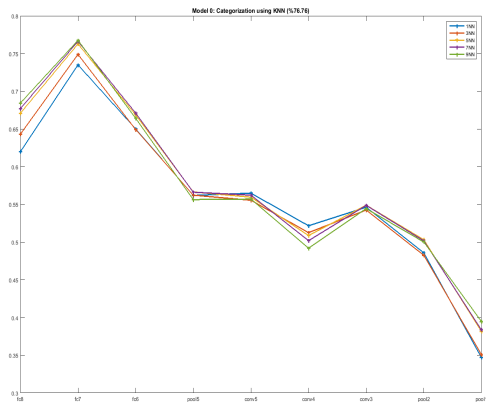


Figure 17: Pascal 3D Model0 KNN performance on Categorization Task

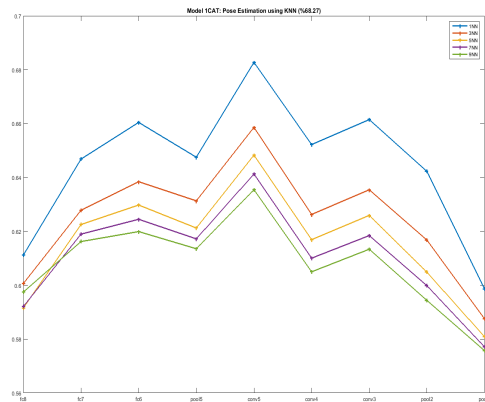


Figure 20: Pascal 3D Model1Cat KNN performance on Pose Estimation Task

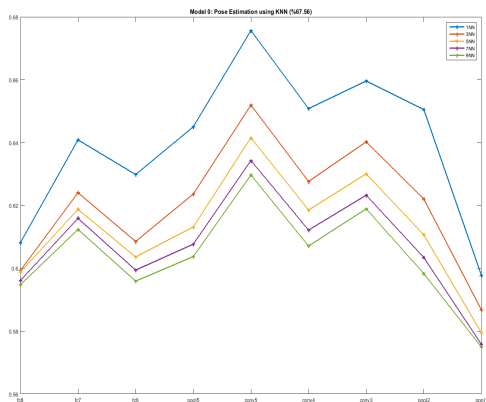


Figure 18: Pascal 3D Model0 KNN performance on Pose Estimation Task

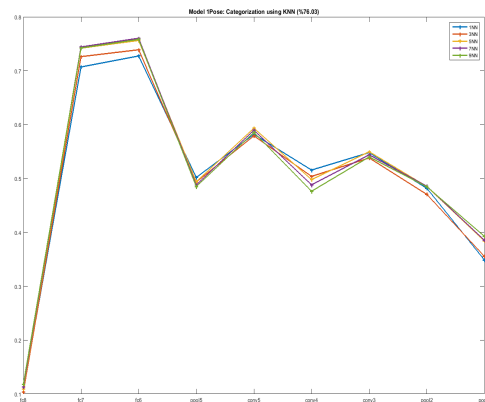


Figure 21: Pascal 3D Model1Pose KNN performance on Categorization Task

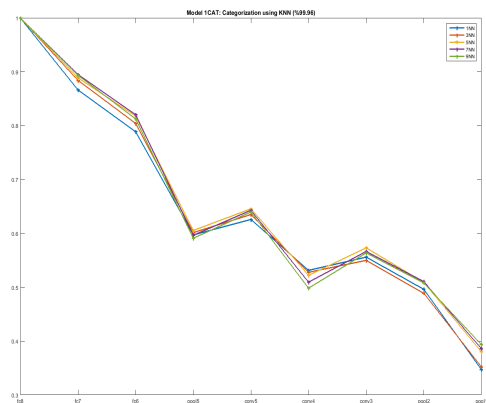


Figure 19: Pascal 3D Model1Cat KNN performance on Categorization Task

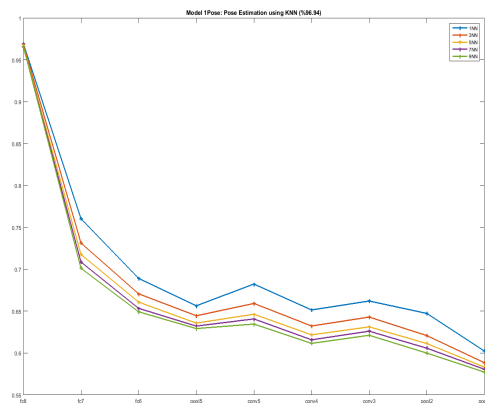


Figure 22: Pascal 3D Model1Pose KNN performance on Pose Estimation Task

maximize the correlation with the output data. We use KPLS to map the affinity matrix of the transformed view-manifold (*view-kernel*) to the circle affinity matrix (*circle-kernel*). Following the convention of the main paper, let the view-kernel is denoted by  $\mathbf{K}^l$ , and the circle-kernel is denoted by  $\mathbf{K}^\circ$  (*The subscript  $n$  is removed to simplify the notation*). We limit the number of extracted PCs to  $d$ , where  $d \ll N$  and  $N$  is the dimensionality of the input kernel (in this work, we use  $d = 5$ ). More specifically, KPLS maps the rows of  $\mathbf{K}^l$  to the rows of  $\mathbf{K}^\circ$ . So that

$$\hat{\mathbf{K}}^\circ = \mathbf{G}_0 \mathbf{U} (\mathbf{T}^\top \mathbf{G}_0 \mathbf{U})^{-1} \mathbf{T}^\top \mathbf{K}^l \quad (4)$$

Where the set of extracted PCs are the columns of the matrix  $\mathbf{T}_{N \times d}$ ,  $\mathbf{U}_{N \times d}$  is auxiliary matrix, and the Gram-matrix  $\mathbf{G}_0$  is defined by

$$\mathbf{G}_0 = \frac{\mathbf{K}^l \mathbf{K}^{l\top}}{b b^\top} \quad (5)$$

Where  $b \in \mathbb{R}^N$ , so that  $b(i)$  is the Frobenius norm of the  $i$ -th row of  $\mathbf{K}^l$ . Based on the mapping in Eq 4, we extract two measurements:

First: *KPLS-Regression Error* ( $\delta$ ) which measures geometric deformation of the generated output image of view-kernel in the circle-kernel space ( $\hat{\mathbf{K}}^\circ$  with respect to the circle-kernel ( $\mathbf{K}^\circ$ ) and the ). One choice for measuring this is

$$\delta(\hat{\mathbf{K}}^\circ, \mathbf{K}^\circ) = 1 - KTA(\hat{\mathbf{K}}^\circ, \mathbf{K}^\circ)$$

Where KTA stands for Kernel Target Alignment (stated in Equation 2 in the main paper). The Regression error measures the reconstruction error of the circle-kernel from the view-kernel.

Second, *KPLS-NormK Ratio* ( $\frac{\|\mathbf{G}_d\|_F}{\|\mathbf{G}_0\|_F}$ ) measure the residual energy after extracting the first  $d$ -PC's. Where  $\mathbf{G}_d$  is the residual of  $\mathbf{G}_0$  after  $d$ -iterations. The intuition behind this measure is that the larger the ratio  $\frac{\|\mathbf{G}_d\|_F}{\|\mathbf{G}_0\|_F}$ , this means that the view-manifold has more than  $d$ -PC's correlated with the circle-kernel.

While KPLS-regression Error is self-explanatory (this measure presented in the main paper), using the two KPLS measurements together gives more precise view on the correlation between the view-manifold and the circle-manifold. From Fig 23b, KPLS-Norm Ratio supports the observation that we noted in the main paper, from Fig 23a, that the lower layers in Model0 are more correlated to the circle-manifold than the higher layers. Except for Pool5, which encodes maximum correlation between the view-manifold and the circle-manifold.

2) *TPS-nonlinearity measure*: In this measure we learn a regularized Thin Plate Spline (TPS) non-linear mapping [7] between the unit circle manifold and each manifold  $\mathcal{M}^k$ . The mapping function ( $\gamma$ ) can be written as

$$\gamma^k(\mathbf{x}) = \mathbf{C}^k \cdot \psi(\mathbf{x}),$$

where  $\mathbf{C}_{d \times (N+e+1)}$  is the mapping matrix,  $e = 2$ , and the vector  $\psi(x) = [\phi(|x - z_1|) \cdots \phi(|x - z_M|), 1, x^T]^T$  represents a nonlinear kernel map from the conceptual representation to a kernel induced space. The thin plate spline is defined as:  $\phi(r) = r^3$  and  $\{z_i\}_{i=1}^M$  are the set of center points. The solution for  $\mathbf{C}^k$  can be obtained by directly solving the linear system:

$$\begin{pmatrix} \mathbf{K}^l + \lambda \mathbf{I} & \mathbf{P}_x \\ \mathbf{P}_t^\top & \mathbf{0}_{(e+1) \times (e+1)} \end{pmatrix}_k \mathbf{C}^{kT} = \begin{pmatrix} \mathbf{A}_k \\ \mathbf{0}_{(e+1) \times d} \end{pmatrix}, \quad (6)$$

$\mathbf{A}$ ,  $\mathbf{P}_x$  and  $\mathbf{P}_t$  are defined for the  $k$ -th set of object images as:  $\mathbf{A}$  is a  $N_k \times M$  matrix with  $\mathbf{K}_{ij}^l = \phi(|x_i^k - z_j|)$ ,  $i = 1, \dots, N_k, j = 1, \dots, M$ ,  $\mathbf{P}_x$  is a  $N_k \times (e+1)$  matrix with  $i$ -th row  $[1, \mathbf{x}_i^{kT}]$ ,  $\mathbf{P}_t$  is  $M \times (e+1)$  matrix with  $i$ -th row  $[1, \mathbf{z}_i^T]$ .  $\mathbf{A}_k$  is a  $N_k \times d$  matrix containing the set of images for manifold  $\mathcal{M}^k$ , i.e.  $\mathbf{A}_k = [\mathbf{y}_1^k, \dots, \mathbf{y}_{N_k}^k]$ . Solution for  $\mathbf{C}^k$  is guaranteed under certain conditions on the basic functions used.

The reason for using TPS in particular is that the mapping has two parts, an affine part (linear polynomial) and a nonlinear part. Inquiring into the two parts gives an impression about the mapping, if it is mostly linear or nonlinear. We used the *reciprocal-condition number* (*RCond*) of the submatrices of the coefficient matrix that correspond to the affine and the nonlinear part.

While Fig 23c shows that the lower layers has more (better) conditioned linear mapping. Fig 23d shows that the lower layer has complete stable mapping. This is expected since the lower layers have high dimensionality. At the same time, Fig 23d shows that the Convolution layers (Conv 3,4 and 5) have unstable nonlinear mappings. An additional observation is that fine-tuning against the pose labels increases the mapping stability (polynomial and non-polynomial). It is clear in Fig 23d that the  $TPS - RCond(CF - nonPoly)$  has very small order of values ( $10^{-11}$ ), therefore, we do not rely on it in our analysis.



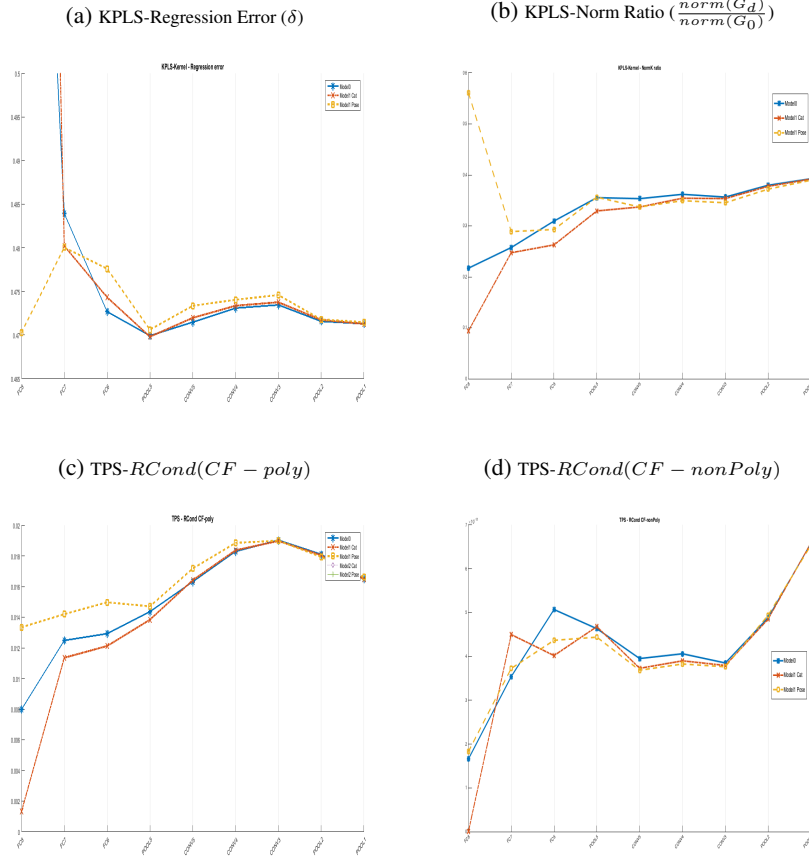


Figure 23: Measurement analysis for the view-manifold in RGBD dataset based on features extracted from different layers of several CNN models. Every figure shows single measurement. Multiple lines is for different CNN model. X-axis is labeled by the layers.